In situ imaging of vortices in Bose-Einstein condensates

Kali E. Wilson, Zachary L. Newman, Joseph D. Lowney, and Brian P. Anderson
College of Optical Sciences, University of Arizona, Tucson, Arizona 85721, USA
(Received 29 May 2014; revised manuscript received 16 January 2015; published 23 February 2015)

We present an application of dark-field imaging that enables *in situ* detection of two-dimensional vortex distributions in single-component Bose-Einstein condensates (BECs). By rotating a ^{87}Rb BEC in a magnetic trap, we generate a triangular lattice of vortex cores in the BEC, with core diameters on the order of 400 nm and cores separated by approximately 9 μm. We have experimentally confirmed that the positions of the vortex cores near the BEC center can be determined without the need for ballistic expansion of the BEC. Our imaging method should allow for the determination of arbitrary distributions of vortices and other superfluid density defects in cases where expansion of the BEC is either impractical or would significantly alter the physical characteristics and appearance of vortices or defects. Our method is also a step toward real-time measurements of complex two-dimensional vortex dynamics within a single BEC.

DOI: 10.1103/PhysRevA.91.023621 PACS number(s): 67.85.De, 42.79.Mt, 67.85.Jk

I. INTRODUCTION

Quantized vortices in superfluids are localized indicators of the superfluid's dynamics. Two-dimensional (2D) vortex distributions are especially relevant in recent experimental efforts to better understand the fluid dynamics of BECs, including vortex dipole and cluster formation [1], 2D quantum turbulence [2,3], formation and decay of persistent currents [2,4–6], and the Berezinskii-Kosterlitz-Thouless transition [7–9]. However, laboratory visualization of vortex cores in a minimally destructive manner that allows for real-time tracking of vortex motion has remained a considerable challenge. Given the submicron size of a vortex core, most experiments involving vortex imaging have relied on a period of ballistic expansion of the BEC prior to image acquisition, limiting observations to a single image of the BEC from trap geometries that support self-similar expansion; see Ref. [10] for an overview of such experiments. Stroboscopic expansion and probing of small fractions of condensed atoms has enabled the determination of few-vortex dynamics in a single BEC [11], although the utility of this technique in measurements of many-vortex dynamics has not yet been established. In order to detect the motions of numerous vortices, as well as to obtain single-shot imaging of vortex distributions in cases where BEC expansion is impractical, new imaging procedures must be explored. Here we demonstrate single-shot *in situ* imaging of a 2D vortex distribution in a rotating BEC, obtained by applying a high-angle dark-field imaging technique that is similar to methods commonly employed in other applications of microscopy [12]. With additional modifications, this imaging method should be amenable to the acquisition of single images of 2D vortex distributions in nonharmonically trapped BECs, and multiple images of a single BEC, offering the potential for experimental determination of the dynamics of 2D vortex distributions.

To date, the most versatile demonstrated method for imaging the dynamics of an arbitrary few-vortex distribution in a BEC is that of Freilich *et al.* [11], in which a few percent of the atoms from a single BEC are pumped into an untrapped state, whereupon they ballistically expand and are probed via absorption imaging. By repeating this extraction procedure, this stroboscopic technique allows for the acquisition of sequential absorption images of a single BEC. However, since it relies on a period of expansion before vortex cores are resolvable, this method may present difficulties in determining the positions of vortices within a tightly packed vortex cluster or in cases where the BEC density distribution does not self-similarly magnify during expansion, such as expansion from a square well potential. Additionally, the required expansion time limits the acquisition rate of these images, making the motion of many vortex cores difficult to track as intervortex distances decrease and cores move more rapidly within the BEC. Minimally destructive, *in situ* observations of vortex dynamics in a single BEC have also been obtained by filling the vortex core with atoms of a different atomic state [13]. Filling the core increases the size of the vortex and enables the position of the core to be determined *in situ* with phase-contrast imaging techniques, but interactions between the two atomic states strongly affect the dynamics of the quantum fluid.

II. DARK-FIELD IMAGING

Our imaging approach involves an adaptation of dispersive dark-field imaging [12]. Conceptually, in dark-field imaging, the BEC is treated as a phase object that coherently refracts light from an imaging probe beam. Briefly, with a monochromatic probe laser beam of approximately uniform intensity I_0 propagating along the z direction, the spatially dependent phase shift $\phi(x,y)$ acquired as the probe passes through the BEC is given by

$$\phi(x,y) = -\tilde{n}(x,y)\sigma_0\left(\frac{\Delta/\Gamma}{1+4(\Delta/\Gamma)^2+I_0/I_{\rm sat}}\right). \quad (1)$$

In this expression, $\tilde{n}(x,y) = \int n(x,y,z)dz$ is the z-integrated column density of the BEC obtained from the full atomic density distribution $n(x,y,z)$, σ_0 is the resonant atom-photon scattering cross section, $\Delta = \omega - \omega_0$ is the detuning of the probe frequency ω from atomic resonance ω_0, Γ is the natural linewidth of the atomic transition, and $I_{\rm sat}$ is the transition saturation intensity. As illustrated in Fig. 1(a), an opaque mask placed on axis in the Fourier plane of an imaging system acts as a high-pass spatial filter, blocking the unrefracted component of the probe beam, but allowing the light refracted by the BEC

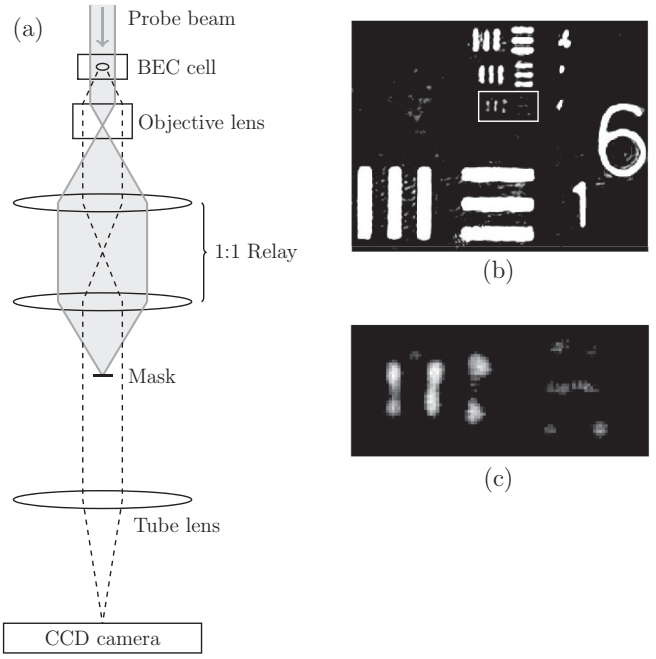

FIG. 1. (a) BEC imaging optics (not to scale). 780-nm probe light (shaded in gray) is directed toward the BEC along the vertical (axial) imaging axis. Light refracted by the BEC (represented by dashed lines) is collected with a microscope objective, and imaged onto the CCD camera. A mask placed in the intermediate Fourier plane of the imaging system provides a high-pass spatial filter. (b) Image of a U.S. Air Force resolution test target, obtained with an offline replica of the imaging system using 780-nm laser light and showing group 6 element 1 (bottom row) and group 7 elements 4–6 (top three rows). (c) Zoomed image of group 7 element 6, the features enclosed in the superimposed white box in (b). These features are the smallest features on our test target, with a width of 2.19 μm and a center-to-center separation of 4.38 μm. The image of the target is used to determine a measured magnification of $M = 19.7 \pm 0.4$, where the error is due to our uncertainty in measuring the periodicity in the test target image. All images obtained with the offline imaging system were taken with a Point Grey Firefly MV CMOS camera with 6×6-μm pixels.

to reach the camera. Andrews *et al.* [14] first applied dispersive dark-field BEC imaging as a minimally destructive alternative to absorption imaging, and demonstrated multishot imaging of a single BEC. More recently, Pappa *et al.* [15] employed near-resonant dark-field imaging to make highly sensitive measurements of the components of a spinor BEC, reporting a detection limit of about seven atoms. In both of these applications of the dark-field technique, the intent was to image the bulk profile of the BEC, rather than locate microscopic density features within the BEC. See the Appendix and Ref. [16] for a more detailed discussion of this imaging method.

We use dark-field imaging to isolate the imaging light scattered by submicron features within the BEC, and in particular to identify the positions of vortex cores. A vortex core is free of condensed atoms, and therefore the core position corresponds to a steep density gradient over a distance on the order of the healing length [17], approximately 400 nm for our parameters. Such a sharply localized density feature acts as a strong lens that refracts light into high spatial frequencies. By carefully selecting the size of the dark-field mask, we remove the low spatial frequencies associated with the more gradual changes in the BEC density profile, allowing primarily the light refracted by the vortex cores to reach the camera. Without the large background signal of the bulk BEC, it is then feasible to pick out the refracted signal due to each vortex core without expanding the BEC. We describe this process as *in situ* vortex imaging due to the ability to detect vortex cores without using a period of ballistic expansion. *In situ* vortex imaging opens the possibility of minimally destructive imaging of vortex distributions, although all BEC imaging procedures are at least somewhat destructive.

III. IMAGING SYSTEM

For the images of vortices reported here, we formed BECs of $5\,^2S_{1/2}\,|F = 1, m_F = -1\rangle\,^{87}$Rb atoms in a magnetic time-averaged orbiting potential (TOP) trap [18], with radial and axial trap frequencies of $(\omega_r, \omega_z) \sim 2\pi \times (8, 16)$ Hz, BEC atom numbers of approximately 1.8×10^6, and BEC Thomas-Fermi radii of $(R_r, R_z) \sim (35, 19)$ μm. Following Hodby *et al.* [19], we modified the TOP trap's rotating bias field to form a slowly rotating elliptical potential well, which in turn spun up the BECs such that a triangular lattice of vortices was formed. The vortex lattice provided a reproducible and easily recognizable pattern of vortex cores for our imaging tests.

As illustrated in Fig. 1(a), our imaging system consists of an infinite-conjugate Olympus SLMPLN 20X microscope objective with a numerical aperture (NA) of 0.25, a theoretical diffraction-limited resolution of 1.9 μm at a wavelength of $\lambda = 780$ nm [20], a working distance of 25 mm, and a focal length of 9 mm. The objective is followed by a 1:1 relay lens pair, composed of two 75-mm focal length achromatic doublets separated by 150 mm. The mask for dark-field imaging is placed at the intermediate Fourier plane, located at the rear focal plane of the relay, between the final relay lens and the tube lens. The relay lens pair is necessary because the initial Fourier plane where the mask would ideally be placed is located within the objective lens housing. Finally, a singlet lens with a focal length of 175 mm is used as the tube lens. All BEC images were obtained with a Princeton Instruments PIXIS 1024 BR back-illuminated CCD camera with 13×13-μm pixels. The imaging system has a magnification of $M = 19.7 \pm 0.4$. We used a variety of dark-field mask shapes and sizes in our imaging tests, described below. For the proof-of-principle tests reported here, the choice of mask shape (circular versus wire) was based on the masks available rather than an optimal shape.

As a first test of the capabilities of our imaging system, we constructed the system offline with a microscope slide in place of the 1-mm-thick glass wall of the vacuum chamber, and imaged a silica nanofiber [21,22] with 660-nm laser light. The nanofiber, with a diameter of approximately 500 nm, provides an example of a submicron phase object with approximately the same diameter as a vortex core, and thus serves as a suitable imaging test object. Figures 2(a)–2(c) show images of the nanofiber obtained by varying dark-field mask size, each image acquired using a 2.5-ms exposure time. The bright-field image shown in Fig. 2(d) is provided for comparison, and was acquired with a 0.25-ms exposure.

Despite its submicron thickness, the nanofiber's position can be clearly determined in both the bright-field and dark-field

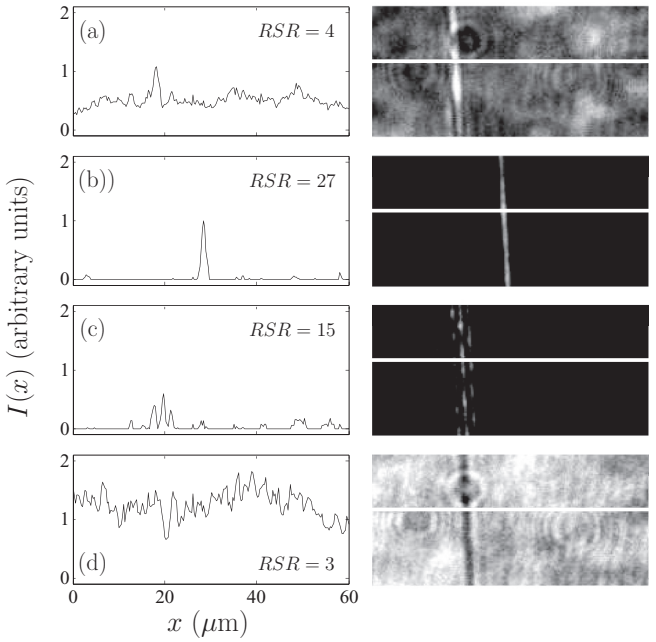

FIG. 2. Raw 60-μm-wide images (right panels) of a section of silica nanofiber with a diameter of ~500 nm (vertically oriented in each image in the panels on the right), shown without the use of background subtraction or other signal-enhancing techniques; 660-nm imaging light was used for all images. Panels on the left show horizontal (x-direction) cross sections through each corresponding image on the right along the white line superimposed on the images; image intensity $I(x)$ is plotted vs x (arbitrary units are the same for each cross section). (a)–(c) Dark-field images taken with a 2.5-ms exposure and using masks with diameters of 100 μm, 370 μm, and ~1.5 mm respectively. Circular masks were used for (a) and (c), whereas a wire mask, aligned approximately parallel to the fiber, was used for (b). (d) Bright-field image of the nanofiber with no mask in place, taken with a 0.25-ms exposure. See text for a discussion of the calculated relative signal ratio (RSR) for the cross sections [23].

images. However, in the bright-field image shown in Fig. 2(d), the detected signal depth from the nanofiber is the same order of magnitude as background features due to the structure on the probe beam and etaloning at the camera, with a relative signal ratio (RSR) of 3, a measure of the signal relative to the variations and noise in the background signal [23]. As shown in Figs. 2(a)–2(c), RSR increases with mask size until the mask begins to alter the profile of the nanofiber signal due to clipping of the lowest spatial frequency components in the refracted signal. Given that the fiber primarily refracts light in the direction perpendicular to its length, we characterize the mask size by the projection of the mask in the direction perpendicular to the fiber. Thus, for a circular mask, or a wire mask oriented parallel to the fiber, the relevant parameter is the mask diameter rather than the actual shape of the mask. The dark-field image of Fig. 2(b) has an RSR of 27, almost an order-of-magnitude improvement over the bright-field image of Fig. 2(d). The 370-μm-diameter wire mask used for the image of Fig. 2(b) is the same wire used for *in situ* vortex imaging described below, and the resulting image of the nanofiber has a full width at half maximum (FWHM) of 1.18 ± 0.03 μm, an approximate measure of the resolution limit of the imaging system rather than the true size of the nanofiber. The FWHM was found by fitting a Gaussian to the intensity profile, and the uncertainty is due to the uncertainty from the fit combined with the uncertainty reported above for the system magnification. For the 660-nm probe wavelength, the calculated diffraction limit of the objective is 1.61 μm [20], which corresponds to a FWHM of 1.36 μm for a diffraction-limited point object. Note that the high-pass spatial frequency filtering inherent in the dark-field imaging process acts to narrow the FWHM of the central intensity peak while increasing the power in the side lobes of the Airy diffraction pattern. Because of this filtering process, it is possible to obtain an image of a point object that has a FWHM that is slightly smaller than the diffraction limit, as we observe. This narrowing of the FWHM is a secondary benefit of dark-field imaging; the primary benefit is the removal of noise inherent in the low spatial frequency signal.

IV. VORTEX IMAGING

Although our ultimate goal is to image arbitrary 2D vortex distributions in highly oblate BECs, we chose a vortex lattice for our initial *in situ* imaging tests because a lattice is an easily recognizable pattern of vortices that can be reliably reproduced. Additionally, the increase in angular momentum due to rotating the BEC causes the BEC's radial width to increase, its axial width to decrease, and the vortices comprising the lattice to align with the rotation and imaging axis. A rotating BEC thus serves as a suitable proof-of-principle test target for investigating the feasibility of imaging arbitrary 2D vortex distributions in highly oblate BECs, which we ultimately intend to study.

As a basis for comparison of the $M \sim 20$ optical system's ability to image vortex distributions, we used our standard, non-diffraction-limited, $M = 5$, NA = 0.2 imaging system to obtain dark-field images of vortices with a BEC after a period of expansion. After spinning up a lattice, turning off the trapping fields, and allowing the BEC to expand for a variable time t_{exp}, we optically pumped the atoms from the $5\,^2S_{1/2}\,|F = 1\rangle$ level to the $|F = 2\rangle$ level and then imaged on the transition to the $5\,^2P_{3/2}\,|F' = 3\rangle$ level. We obtained images of vortex cores using both dark-field imaging, as shown in Figs. 3(a)–3(d), and standard bright-field absorption imaging, as shown in Fig. 3(e). A circular mask with a diameter of ~1.6 mm was used for all of the dark-field images shown in Fig. 3, and the probe detuning ranged from -1Γ to -2Γ from the $|F = 2\rangle$ to $|F' = 3\rangle$ hyperfine transition. As shown in Figs. 3(a)–3(d), vortex core resolvability increased for longer expansion times. The low magnification and NA of the imaging system limited our ability to resolve two neighboring cores for expansion times less than about 30 ms. While cores may be resolvable at expansion times less than 30 ms, the corresponding smaller atom cloud should result in a higher percentage of the light refracted from the bulk BEC bypassing the mask, thereby reducing contrast between vortex cores and the bulk BEC in the absence of further optimization of mask size.

To image vortex cores within a *trapped* BEC, we used the $M \sim 20$, NA = 0.25 imaging system previously described. Representative *in situ* dark-field images of a BEC confined within the TOP trap are shown in Fig. 4. The dark-field images show a clear distinction between a BEC without a vortex

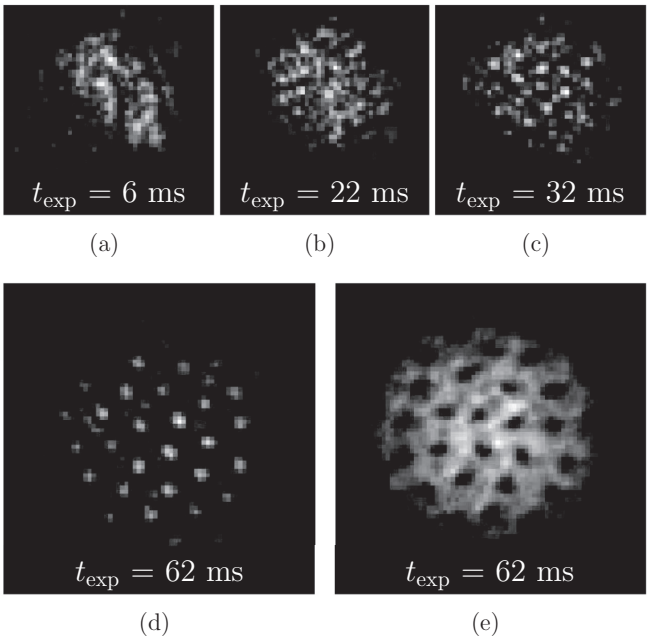

FIG. 3. Images of expanded BECs with a vortex lattice, using an $M = 5$, NA $= 0.2$ imaging system. (a)–(c) show a 135-μm-wide field of view, and (d) and (e) show a 200-μm-wide field of view. For each image, the BEC was released from the trap and allowed to expand for a variable time t_{exp} shown on the image. (a)–(d) Raw dark-field images of an expanded BEC with a vortex lattice taken at varying expansion times, with no background subtraction. A circular mask with diameter of ∼1.6 mm was used for all dark-field images. The lattice becomes resolvable between $t_{exp} = 22$ and 32 ms. (e) Reference absorption image of an expanded BEC with a vortex lattice, obtained using standard methods of bright-field imaging with background subtraction and grayscale contrast inversion.

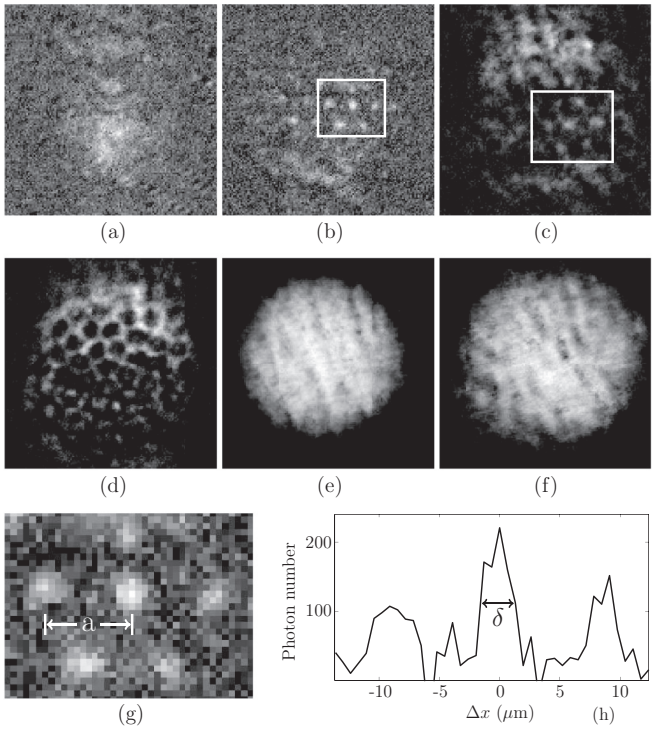

FIG. 4. (a)–(f) 80-μm-wide *in situ* images of BECs obtained with our $M \sim 20$, NA $= 0.25$ imaging system. Dark-field images of the BEC are shown (a) without a vortex lattice and (b) with a vortex lattice. The wire mask used for both images had a diameter of 370 μm, and was aligned horizontally with respect to the image. (c) Dark-field image of a BEC with a vortex lattice, but with a 250-μm-diameter wire mask; vortices are visible within the superimposed white rectangle, but not as apparent as in (b), as additional refracted light from the BEC reaches the camera. (d) Dark-field image obtained with a rotating BEC with a vortex lattice when the imaging system is not properly focused. All dark-field images have been processed by subtraction of a background image taken in the absence of a BEC. Reference *in situ* absorption images are shown for (e) a nonrotating BEC and (f) a rotating BEC that is expected to contain vortices. Bright-field images were obtained using standard methods of bright-field imaging with background subtraction and grayscale contrast inversion. (g) Magnified view of the region bounded by the white rectangle in (b), with pixelation due to the 13×13-μm camera pixels. Neighboring vortex cores are separated by $a \sim 9$ μm. (h) Cross section along the middle row of vortex cores shown in (e); the vertical scale is proportional to image intensity per pixel, calibrated to number of photons; the horizontal plot axis shows the distance Δx away from the central vortex core, with the scale corresponding to real distances at the object plane. The FWHM of the central vortex core is $\delta = 2.4 \pm 0.5$ μm. The FWHM was found by fitting a Gaussian to the intensity profile, and the reported error is due to the uncertainty from the fit.

lattice, Fig. 4(a), and one with a lattice, Figs. 4(b)–4(d). For comparison, an *in situ* bright-field image of a BEC without a vortex lattice and an image of a BEC with a vortex lattice are shown in Figs. 4(e) and 4(f), respectively. Unlike the dark-field vortex lattice images, Fig. 4(f) shows no clear vortex cores, as it is difficult to distinguish between the weak transmission feature corresponding to a vortex core and structure on the probe beam or other imaging artifacts. For the images in Figs. 4(a)–4(c), we used an imaging probe with a $1/e^2$ beam radius of ∼2 mm, a power of ∼0.5 mW, a detuning of $\Delta = 4.5\Gamma$ from the $|F = 2\rangle$ to $|F' = 3\rangle$ transition, and an exposure time of 20 μs. For the vortex lattice shown in Fig. 4(b), we measured the separation between vortex cores to be $a \sim 9$ μm, as shown in Fig. 4(g). The FWHM of the central vortex core of Fig. 4(g), as determined from the cross section given in Fig. 4(h), was measured to be $\delta = 2.4 \pm 0.5$ μm, indicating that the imaging system should be capable of resolving two vortex cores separated by approximately this distance. The FWHM is a measure of the point-spread function for our imaging system rather than the actual size of the vortex core. The detuning was chosen to maximize the signal from the vortex cores for the 370-μm-diameter mask. Such close detuning was destructive to the BEC, and with these parameters we are limited to acquiring a single image per BEC. Additionally, due to the low signal level of these images, we utilized background subtraction to remove features due to the unrefracted probe light that were not obstructed by the mask.

As discussed, the size of the dark-field mask determines the spatial frequency cutoff of the spatial filter. Figure 4(c) shows a dark-field image taken using a mask diameter of 250 μm. The smaller mask size allows more of the light refracted from the bulk BEC to reach the camera, reducing

the contrast of the vortex cores. In comparison, the 370-μm-diameter wire mask used for Fig. 4(b) blocks almost all of the light refracted by the bulk BEC. Figure 4(d) shows a representative out-of-focus image of a vortex lattice, obtained with a detuning of $\Delta = 4\Gamma$ and a 30-μs exposure. The lattice takes on a honeycomb appearance similar to that observed in an out-of-focus bright-field absorption image of a vortex lattice. Note that with the exception of the out-of-focus lattice we primarily see vortex cores in the center of the BEC. We speculate that this could be due to the decrease in density at the edge of the BEC, and correspondingly smaller angles of refraction associated with the vortex cores, due to the increase in healing length and decrease of integrated optical density along the probe propagation direction. Additionally, the use of a wire mask introduces an asymmetry in the background signal since all spatial frequencies are blocked in the direction parallel to the wire. For the results presented here, the choice to use a wire mask instead of a circular mask was based on the masks available; given the radial symmetry of the BEC, a circular mask is preferable. We anticipate that using a precision circular mask with an optimized size, and imaging vortices in BECs held in a flat-bottomed potential [24], will improve our ability to detect vortices across the BEC.

V. CONCLUSIONS AND OUTLOOK

The single-shot, *in situ* images of bare vortex cores presented here serve as a promising proof-of-principle indication that complex vortex dynamics may be measurable in trapped BECs with additional optimization of the imaging system and imaging parameters. In numerical studies of 2D quantum turbulence, our particular area of interest, vortex-antivortex annihilation and bound pairs of vortices of the same sign of circulation appear to show minimum intervortex separation distances of approximately 2 μm for our parameters [2]. Resolutions approaching this scale are already achievable with our imaging system.

The primary hurdle in extending this technique to capturing multiple images of a single BEC is the achievement of a sufficient RSR, given the large probe detuning and low probe intensity desired for minimally destructive imaging. While the Olympus objective used for the imaging system reported here appears to be a suitable commercial objective given the physical constraints of our apparatus, this microscope objective is optimized for visible light, and its transmission is approximately 60% for our operating wavelength of 780 nm. Additionally, the relay lenses required to place the mask in an accessible intermediate Fourier plane introduce aberrations to the imaging system, making it more difficult to block all of the weakly scattered imaging light and obtain the best possible RSR.

We are currently implementing modifications to the imaging system that should improve both the image quality and the RSR. We are installing a custom objective, optimized for 780-nm imaging probe light, with an accessible rear focal plane, based on the design of Ref. [25]; we have measured the transmission of this objective to be 88% at 780 nm. We also anticipate that using a CCD camera with electron multiplying (EMCCD) gain capabilities, in conjunction with dark-field imaging, will result in a significant increase in the overall signal-to-noise ratio, and will enable the use of imaging light further detuned from resonance. Recently Gajdacz *et al.* have used an EMCCD camera and dark-field Faraday imaging to obtain thousands of images of a single BEC [26]. In situations with low signal, but also low background light levels, the prereadout amplification of an EMCCD camera should be beneficial in imaging vortex distributions.

One significant advantage of dark-field imaging is the minimization of background light, allowing for weak signals to be obtained and amplified without the need for background image subtraction. This potential advantage will be especially useful for measurements of vortex dynamics where the time between images is expected to be on the order of 10 ms. In the dark-field *in situ* images presented here, background image subtraction was necessary due to low vortex signal levels and relatively high levels of weakly scattered probe light reaching the camera, and further optimization of the probe beam profile and dark-field mask will be necessary to utilize raw images without the need for background subtraction, and to take advantage of the prereadout amplification of an EMCCD camera.

Numerical calculations for the propagation of the dark-field signal due to a BEC containing a central vortex are discussed in detail in the Appendix. Our calculations assume propagation through an imaging system with a magnification of $M = 11$, with a probe beam that is tuned near the $|F = 1\rangle$ to $|F' = 2\rangle$ transition. Our calculations indicate that, for a probe detuning of $\Delta = +200$ MHz, a probe intensity of $I = 6.4\,\mathrm{W/m^2}$, an exposure time of 50 μs, a dark-field mask of radius 520 μm, and an assumed transmission of 75%, vortex signals should be on the order of 160 photons on a central 16×16-μm square camera pixel. For these same parameters, the maximum signal from the bulk BEC should be on the order of ten photons per pixel. We have tested the destructiveness of these imaging probe parameters and found that after eight images approximately 50% of the atoms remain. Given our demonstrated capability to observe vortex signals with photon numbers on the order of 200 photons per pixel with a non-electron-multiplying CCD camera as shown in Fig. 4(h), we anticipate that the imaging parameters used for our numerical calculations should yield experimentally observable vortex cores in at least two or three images, with further optimization likely with EMCCD cameras that are sensitive to much lower signal levels than the target signal levels of this numerical study.

We have demonstrated single-shot *in situ* imaging of vortex cores in a BEC. Based on this result and our numerical calculations, we anticipate that the improvements detailed here will enable the ability to obtain multishot, *in situ* imaging of vortices and their dynamics within a single BEC, and to obtain images of vortex distributions in BECs that cannot be readily determined from images after ballistic expansion. Access to such images will open up new possibilities for experiments to study numerical and theoretical predictions of 2D quantum turbulence [27–30], our primary goal, and an even wider range of superfluid dynamics, such as shock wave and soliton dynamics.

ACKNOWLEDGMENTS

We acknowledge the support of the U.S. NSF Grant No. PHY-1205713. K.E.W. acknowledges support from the

Department of Energy Office of Science Graduate Fellowship Program, administered by ORISE-ORAU under Contract No. DE-AC05-06OR23100. K.E.W., J.D.L., and Z.L.N. acknowledge support from the University of Arizona TRIF Program. We thank Olympus for the loan of the microscope objective, Pascal Mickelson and Poul Jessen for providing the nanofiber, and Tom Milster for helpful suggestions.

APPENDIX

Here we provide a detailed description of our numerical methods used to calculate the expected vortex signal that would be obtained using the imaging method described in the text, assuming a single vortex is present at the center of a BEC held in a radially symmetric oblate harmonic trap.

1. BEC density profile

We first consider a BEC without a vortex. The BEC is assumed to have a three-dimensional density distribution:

$$n(r,z) = \begin{cases} n_0\left(1 - r^2/R_r^2 - z^2/R_z^2\right) & r^2/R_r + z^2/R_z^2 < 1 \\ 0 & \text{otherwise} \end{cases} \tag{A1}$$

where z is the axial coordinate corresponding to the imaging axis, r is the radial coordinate at the BEC, R_r and R_z are radial and axial Thomas-Fermi radii, and n_0 is the peak BEC density. When integrated along z, this density distribution leads to a two-dimensional integrated column density distribution:

$$\tilde{n}_c(r) = \begin{cases} n_{2D}(1 - r^2/R_r)^{3/2} & r \leqslant R_r \\ 0 & r > R_r \end{cases} \tag{A2}$$

where $n_{2D} = 5N/2\pi R_r^2$, with N the number of condensed atoms.

With a vortex in the center of the BEC, we assume an integrated column density distribution of $\tilde{n}_v(r) = \chi(r)\tilde{n}_c(r)$, where

$$\chi(r) = \frac{r^2}{r^2 + (\xi/\Lambda)^2}, \tag{A3}$$

ξ is the BEC healing length calculated for peak density n_0, and $\Lambda \approx 0.825$ is a constant that ensures the vortex density distribution has the analytically obtained exact slope near the center of the vortex core [27]. We neglect both the variation of the healing length along the axial direction as well as modifications to the overall BEC shape due to the presence of the vortex, except near the center of the BEC where the vortex is located.

2. Phase shift acquired due to the BEC

Following the method of Ref. [16], we treat the BEC as a thin lens. A monochromatic laser with electric-field amplitude E_0 incident on the BEC acquires a phase shift

$$\phi = -\tilde{n}(r)\sigma_0\left(\frac{\Delta/\Gamma}{1 + 4(\Delta/\Gamma)^2 + I_0/I_{\text{sat}}}\right) \tag{A4}$$

and is attenuated by

$$\alpha = \frac{-\tilde{n}(r)\sigma_0}{2}\left(\frac{1}{1 + 4(\Delta/\Gamma)^2 + I_0/I_{\text{sat}}}\right), \tag{A5}$$

such that the field after passing through the BEC is

$$E = tE_0e^{i\phi} \tag{A6}$$

where $t = e^{\alpha}$. In these expressions, $\tilde{n}(r)$ is the integrated column density $\tilde{n}_c(r)$ (if a vortex is not present) or $\tilde{n}_v(r)$ (if a vortex is present), σ_0 is the resonant atom-photon cross section, $\Delta = \omega - \omega_0$ is the probe detuning from resonance, Γ is the natural linewidth of the transition, I_0 is the incident probe intensity (assumed to be constant), and I_{sat} is the saturation intensity of the atomic transition. For dark-field imaging, the mask in the Fourier plane blocks the probe light such that the dark-field electric field E_{DF} reaching the camera is

$$E_{\text{DF}} = E_0(te^{i\phi} - 1). \tag{A7}$$

3. Propagation through the imaging system

In the Fresnel diffraction regime, with a radially symmetric field, the propagation of light from the front focal plane to the rear focal plane of a thin lens is represented by

$$\begin{aligned} E_{\text{RFP}}(\rho) = \frac{4\pi^2}{\lambda^2 f^2}e^{i\pi\rho^2/\lambda f}\int_0^\infty we^{i\pi w^2/\lambda f} \\ \times\left[\int_0^\infty rE_{\text{FFP}}(r)e^{i\pi r^2/\lambda f}J_0\left(\frac{2\pi wr}{\lambda f}\right)dr\right] \\ \times P(w)J_0\left(\frac{2\pi\rho w}{\lambda f}\right)dw, \end{aligned} \tag{A8}$$

where $E_{\text{FFP}}(r)$ is the initial field at the front focal plane of the lens, $E_{\text{RFP}}(\rho)$ is the final field at the rear focal plane, $P(w)$ is the pupil function of the lens and accounts for the finite numerical aperture of the lens, f is the focal length of the lens, λ is the wavelength of the light, J_0 is the zeroth-order Bessel function of the first kind, and ρ and w are radial coordinates in the rear focal plane and at the lens, respectively [31]. As shown in Fig. 5, the imaging system is configured such that the rear focal plane of the objective lens is coincident with the front focal plane of the tube lens. Propagating the incident field E_{DF} through this system consists of applying Eq. (A8) with $f = f_{\text{obj}}$, the focal length of the objective, to propagate from the object plane to the Fourier plane.

In the Fourier plane, we apply the mask

$$M(\rho) = \begin{cases} 0 & \rho \leqslant \rho_M \\ 1 & \rho > \rho_M \end{cases} \tag{A9}$$

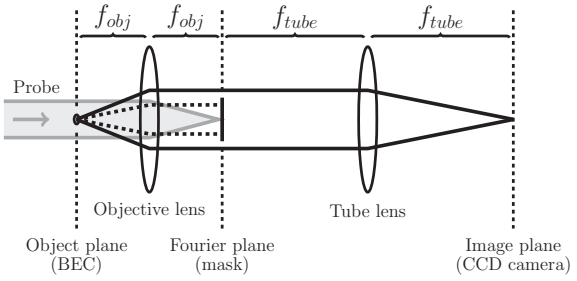

FIG. 5. Basic imaging system with the probe beam shown in gray (not to scale). Horizontal dashed lines indicate light refracted by the bulk BEC into low spatial frequencies. Solid lines indicate light refracted by vortex cores into high spatial frequencies.

where $M(\rho)$ is effectively a high-pass spatial filter with a spatial frequency cutoff of $\rho_M/\lambda f_{\rm obj}$ that is multiplied by the field obtained for the Fourier plane. Lastly we apply Eq. (A8) again, this time with $f = f_{\rm tube}$, the focal length of the tube lens, to propagate the filtered field from the Fourier plane to the image plane located at the CCD camera.

4. Vortex signal

Figure 6 shows the calculated number of photons per 16×16-μm camera pixel for a dark-field image of a BEC with a vortex (filled circles) and one without a vortex (open squares). The signal was calculated using the propagation method outlined in Sec. 3 of the Appendix with $\lambda = 780$ nm, $f_{\rm obj} = 36$ mm, $f_{\rm tube} = 400$ mm, $\rho_M = 520\ \mu$m, $N = 2 \times 10^6$ atoms, $R_r = 49\ \mu$m, $R_z = 7\ \mu$m, $\xi = 325$ nm, and $I_{\rm sat} = 32\ {\rm W/m^2}$. Photon numbers correspond to the probe parameters $\Delta = +200$ MHz, $I_0 = 6.4\ {\rm W/m^2}$, an exposure time of 50 μs, and an estimated 75% transmission through the optical system. The maximum photon signal corresponding to the center of the vortex is 160 photons, whereas the signal for the central BEC pixel is ten photons.

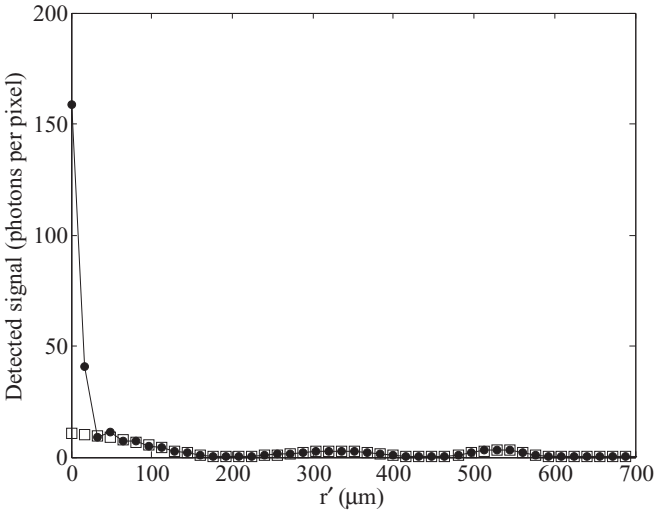

FIG. 6. Detected signal, in the number of photons expected to fall on a 16×16-μm region centered at a location r' away from the center of the image. The calculated signals due to a BEC with a vortex (filled circles) and one without a vortex (open squares) are shown. The parameters used in this calculation are those described in the text.

[1] T. W. Neely, E. C. Samson, A. S. Bradley, M. J. Davis, and B. P. Anderson, Phys. Rev. Lett. **104**, 160401 (2010).

[2] T. W. Neely, A. S. Bradley, E. C. Samson, S. J. Rooney, E. M. Wright, K. J. H. Law, R. Carretero-González, P. G. Kevrekidis, M. J. Davis, and B. P. Anderson, Phys. Rev. Lett. **111**, 235301 (2013).

[3] W. J. Kwon, G. Moon, J.-Y. Choi, S. W. Seo, and Y.-I. Shin, Phys. Rev. A. **90**, 063627 (2014).

[4] S. Moulder, S. Beattie, R. P. Smith, N. Tammuz, and Z. Hadzibabic, Phys. Rev. A **86**, 013629 (2012).

[5] K. C. Wright, R. B. Blakestad, C. J. Lobb, W. D. Phillips, and G. K. Campbell, Phys. Rev. Lett. **110**, 025302 (2013).

[6] K. J. H. Law, T. W. Neely, P. G. Kevrekidis, B. P. Anderson, A. S. Bradley, and R. Carretero-González, Phys. Rev. A **89**, 053606 (2014).

[7] Z. Hadzibabic, P. Krüger, M. Cheneau, B. Battelier, and J. Dalibard, Nature (London) **441**, 1118 (2006).

[8] R. Desbuquois, L. Chomaz, T. Yefsah, J. Léonard, J. Beugnon, C. Weitenberg, and J. Dalibard, Nature Physics **8**, 645 (2012).

[9] J. Y. Choi, S. W. Seo, and Y. I. Shin, Phys. Rev. Lett. **110**, 175302 (2013).

[10] B. P. Anderson, J. Low Temp. Phys. **161**, 574 (2010).

[11] D. V. Freilich, D. M. Bianchi, A. M. Kaufman, T. K. Langin, and D. S. Hall, Science **329**, 1182 (2010).

[12] G. S. Settles, *Schlieren and Shadowgraph Techniques: Visualizing Phenomena in Transparent Media* (Springer-Verlag, Berlin, 2001).

[13] B. P. Anderson, P. C. Haljan, C. E. Wieman, and E. A. Cornell, Phys. Rev. Lett. **85**, 2857 (2000).

[14] M. R. Andrews, M.-O. Mewes, N. J. van Druten, D. S. Durfee, D. M. Kurn, and W. Ketterle, Science **273**, 84 (1996).

[15] M. Pappa, P. C. Condylis, G. O. Konstantinidis, V. Bolpasi, A. Lazoudis, O. Morizot, D. Sahagun, M. Baker, and W. von Klitzing, New J. Phys. **13**, 115012 (2011).

[16] W. Ketterle, D. Durfee, and D. Stamper-Kurn, in *Bose-Einstein Condensation in Atomic Gases, Proceedings of the International School of Physics "Enrico Fermi" Vol. 140*, edited by M. Inguscio, S. Stringari, and C. Wieman (IOS, Amsterdam, 1999), p. 67.

[17] C. Pethick and H. Smith, *Bose-Einstein Condensation in Dilute Gases*, 2nd ed. (Cambridge University, Cambridge, 2008).

[18] W. Petrich, M. H. Anderson, J. R. Ensher, and E. A. Cornell, Phys. Rev. Lett. **74**, 3352 (1995).

[19] E. Hodby, G. Hechenblaikner, S. A. Hopkins, O. M. Maragò, and C. J. Foot, Phys. Rev. Lett. **88**, 010405 (2001).

[20] The diffraction-limited resolution R of the microscope objective is calculated using the Rayleigh criterion, $R = 0.61\lambda/NA$. While this criterion is defined for incoherent light it still provides a useful estimate of resolution when using coherent light.

[21] A. Stiebeiner, R. Garcia-Fernandez, and A. Rauschenbeutel, Opt. Express **18**, 22677 (2010).

[22] E. Vetsch, D. Reitz, G. Sague, R. Schmidt, S. T. Dawkins, and A. Rauschenbeutel, Phys. Rev. Lett. **104**, 203603 (2010).

[23] RSR is the average of all the $RSR_{\rm cross}$ values calculated for individual cross sections perpendicular to the nanofiber orientation. $RSR_{\rm cross} = |I_{\rm sig} - \bar{I}_{\rm BG}|/\sigma_{\rm BG}$, where $I_{\rm sig}$ is the pixel value corresponding to the position of the nanofiber, $\bar{I}_{\rm BG}$ is the average pixel value, and $\sigma_{\rm BG}$ is the standard deviation. When calculating $\bar{I}_{\rm BG}$ and $\sigma_{\rm BG}$, the 14 pixels on either side of the signal peak are not used.

[24] A. L. Gaunt, T. F. Schmidutz, I. Gotlibovych, R. P. Smith, and Z. Hadzibabic, Phys. Rev. Lett. **110**, 200406 (2013).

[25] W. Alt, Optik **113**, 142 (2002).

[26] M. Gajdacz, P. L. Pedersen, T. Mørch, A. J. Hilliard, J. Arlt, and J. F. Sherson, Rev. Sci. Instrum. **84**, 083105 (2013).

[27] A. S. Bradley and B. P. Anderson, Phys. Rev. X **2**, 041001 (2012).

[28] A. C. White, C. F. Barenghi, and N. P. Proukakis, Phys. Rev. A **86**, 013635 (2012).

[29] M. T. Reeves, T. P. Billam, B. P. Anderson, and A. S. Bradley, Phys. Rev. Lett. **110**, 104501 (2013).

[30] T. P. Billam, M. T. Reeves, B. P. Anderson, and A. S. Bradley, Phys. Rev. Lett. **112**, 145301 (2014).

[31] J. Goodman, *Introduction to Fourier Optics*, 3rd ed. (Roberts and Company, Greenwood Village, CO, 2005).